PAPER

Check for updates

Phases and excitations of active rod–bead mixtures: simulations and experiments†

Harsh Soni,*[ab] Nitin Kumar,[ac] Jyothishraj Nambisan,[ad] Rahul Kumar Gupta,[b] A. K. Sood[a] and Sriram Ramaswamy [iD][ab]

We present a large-scale numerical study, supplemented by experimental observations, on a quasi-two-dimensional active system of polar rods and spherical beads confined between two horizontal plates and energised by vertical vibration. For a low rod concentration Φ_r, our observations are consistent with a direct phase transition, as bead concentration Φ_b is increased, from the isotropic phase to a homogeneous flock. For Φ_r above a threshold value, an ordered band dense in both rods and beads occurs between the disordered phase and the homogeneous flock, in both experiments and simulations. Within the size ranges accessible, we observe only a single band, whose width increases with Φ_r. Deep in the ordered state, we observe broken-symmetry "sound" modes and giant number fluctuations. The direction-dependent sound speeds and the scaling of fluctuations are consistent with the predictions of field theories of flocking; sound damping rates show departures from such theories, but the range of wavenumbers explored is modest. At very high densities, we see phase separation into rod-rich and bead-rich regions, both of which move coherently.

1 Introduction

Active matter is the focus of intense current interest due to its dramatic mechanical and statistical properties,[1–4] such as giant number fluctuations,[5–8] wave propagation without conventional inertia,[8–11] broken continuous symmetry in two dimensions, band formation,[12–14] sustained spontaneous oscillations, instability of simple liquid-crystalline order in bulk fluid,[15] motile topological defects,[6,7,16–21] motility-induced phase separation and its generalisations[22–25] and viscosity reduction through internally generated stresses.[26–28] The origin of these properties is the energy supply at the microscopic level, directly to the constituent particles, unlike in conventional nonequilibrium systems such as sheared fluids, which are powered through their periphery. The energy transduction responsible for the active character of a particle could be wholly internal, as in living organisms,[29–31] or it could take place in the region of contact of the particle with its surroundings, as with self-phoretic

colloids in a fluid,[32] Quincke rollers[33] or vibrated grains.[6,34,35] Active particles are commonly elongated and can therefore form orientationally ordered states, of which the simplest are nematic and polar uniaxial liquid crystals. Diverse mechanisms underlie the ordering of active particles: in living active systems like bird flocks,[36] fish schools and herds, the process is behavioural and based on mutual sensing. In active granular systems, which exemplify dry active matter,[37] steric and collisional effects give rise to alignment.[6,38] In colloidal rollers, a restricted version of the hydrodynamic interaction is responsible.[33]

Considerable progress has been made towards understanding active polar systems since the discovery of a flocking phase transition in an agent-based model,[39] including field-theoretic arguments towards the existence of long-range order in 2D flocks,[3,8,11,40,41] and predictions of highly anisotropic sound waves – through the interplay of the concentration and broken-symmetry fields – and anomalously large number fluctuations in the ordered phase.[3,8,9] Recently, Geyer *et al.*[10] observed sound waves in the suspension of active colloidal rollers. Bertin *et al.*,[42] in a Boltzmann-equation construction of the Toner–Tu equations, discovered that the dependence of the local ordering tendency on the local density inevitably led to a linear instability of the ordered phase, with wavevectors parallel to the ordering direction, just past the mean-field flocking transition. Indeed, a banded phase is widely observed to intervene between the isotropic and the uniform ordered phases in agent-based numerical simulations[12–14] and in experiments on rolling-colloid flocks,[33] and arises as well in a variety of theoretical models.[43–45]

a Department of Physics, Indian Institute of Science, Bangalore 560 012, India. E-mail: harshiisc@gmail.com

b TIFR Centre for Interdisciplinary Sciences, Tata Institute of Fundamental Research, Hyderabad 500 107, India

c Department of Physics, Indian Institute of Technology Bombay, Powai, Mumbai 400 076, India

d School of Physics, Georgia Institute of Technology, 770 State Street NW, Atlanta, GA, 30332-0430, USA

† Electronic supplementary information (ESI) available. See DOI: 10.1039/c9sm02552a

Here, we study a two-dimensional active polar monolayer consisting of tapered rods adrift in a sea of spherical beads. The energy input to the particles is provided by a vertically vibrated supporting surface, and the rods, by virtue of their shape, transduce this vibration into directed movement in the plane. The spherical beads mediate an aligning interaction between the rods, and otherwise behave like passive particles that move if pushed or dragged by the polar rods. In earlier work on this system,[35,46,47] we discovered a nonequilibrium phase transition from the isotropic state to an ordered, coherently moving flock, which took place when the concentration of the spherical beads exceeded a critical value that decreased with increasing concentration of rods. Our experimental results were supported by a hydrodynamic theory and numerical simulations incorporating the detailed Newtonian mechanics of the particles and boundaries, including vibration, inelasticity and static friction. In this paper, we offer a detailed exploration of the phase diagram, mode structure and spatiotemporal correlations of this system, primarily in simulations but supported by key experimental findings. There are of course many parameters one could consider varying, such as the concentrations of rods and beads, the rotational diffusivity of the rods, and coefficients of friction between the particles and the substrate, several of which feed into the speed of the rods, and thus mainly change the effective clock speed of the dynamics. We restrict our studies to the dependence on rod area fraction Φ_r and the bead area fraction Φ_b. Our numerical studies all employ periodic boundary conditions (PBCs) in the horizontal plane, thus eliminating the role of the lateral boundaries of the sample. In principle, our system is distinct from a single-component Vicsek model because it has two conserved species, and is also distinct from confined flocks in incompressible fluid[33,48] because the bead fluid is compressible and its density is a relevant control parameter.

Here is a summary of our main results. (i) Large-scale simulation studies over a range of Φ_r and Φ_b, under periodic boundary conditions, reveal that a banded state intervenes between the isotropic state and the homogeneous ordered phase, for Φ_r above a threshold value Φ_r^c, as Φ_b is increased. For the system sizes we explored, even for a long-channel geometry with the aspect ratio as large as 16, we see a single coherently moving band rich in both rods and beads, and not a periodic array. We cannot of course say if an even larger simulation will reveal a long-period striped state as in ref. 14. Detailed studies of band morphology can be found in the body of the paper. Below Φ_r^c, the system appears, within our resolution, to undergo a phase transition from a disordered to an ordered state directly, as discussed in ref. 35. (ii) We present experimental evidence for a banded flock, to our knowledge for the first time in dry granular matter. (iii) In the homogeneous ordered state, our numerical studies reveal giant number fluctuations and a spectrum of propagating modes. The observed wavevector dependence of the damping rates of the modes differs from the predictions of the Toner–Tu theory, which does however capture other broad features such as the scaling of the number fluctuations, and direction-dependent wavespeeds. (iv) At higher values of total concentration of the rods and the beads, we observe phase segregation into bead-rich and aligned rod-rich regions, both moving coherently. The remainder of the paper is organised as follows: in Section 2, we discuss our numerical and experimental methods. In Section 3, we present our detailed results. We summarise and suggest future directions in the last Section 4.

2 Methods

2.1 Experiment

Our experimental cell has a shallow circular geometry, made of hardened aluminium alloy. The particles are confined to two dimensions using a glass lid, which is fixed on the external perimeter of the circle at a height of $w = 1.2$ mm above the base. We use the "flower" geometry[35,49] to prevent clustering of particles on the cell boundary. The cell is mounted on a permanent magnet shaker (LDS 406/8) and is shaken at a fixed frequency $f = 200$ Hz and amplitude a_0. The amplitude of the resulting sinusoidal acceleration $\Gamma \equiv a_0(2\pi f)^2/g$, measured by an accelerometer (PCB Piezoelectronics 352B02), is chosen to be 7.0 in the units of the gravitational acceleration of the earth g. Our "self-propelled" polar particle, which we call a "rod" henceforth, is a brass rod, $\ell = 4.5$ mm long and 1.1 mm in diameter at its thick end, as shown in Fig. 1(a). The tilt of the rod with respect to the horizontal transduces the energy of vertical vibration into in-plane propulsion, and its geometrical polarity, that is, fore-aft asymmetry, ensures that this propulsion is biased towards one end of the rod, specifically the narrow end. The other particles in our experiment are spherical beads of aluminium, 0.8 mm in diameter, which do not show any in-plane dynamics when vibrated vertically. We created an annular geometry by inserting a circular disk of 5 cm diameter in the middle of the experimental cell. We expected this geometry to stabilize flocking along the azimuthal direction and therefore to favour bands.
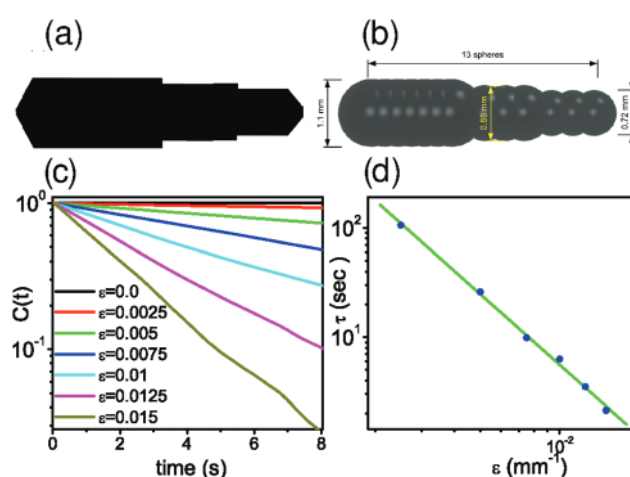

Fig. 1 (a) A schematic diagram of the experimental rod. (b) Simulated rod made of 13 spheres overlapping with each other. (c) Orientation autocorrelation function $C(t)$ of a single rod in simulations *vs.* t for different values of ε. Clearly, $C(t) \sim \exp(-t/\tau)$. (d) Relaxation time τ as a function of ε, shown as ε^{-2} dependence.

2.2 Simulation

Our numerical simulations are based on a mechanically faithful reproduction of the microscopic dynamics of each particle. We assume that all the particles and walls are perfectly rigid. Therefore, all interactions are instantaneous events. All the collisions are inelastic with prescribed restitution and Coulomb friction, and the gravitational acceleration of the earth is taken into account in our simulations. The vibrating base and lid are modelled as horizontal walls moving in the vertical direction with their z-coordinates changing with time t as $a_0 \cos 2\pi f t + a_0$ and $a_0 \cos 2\pi f t + a_0 + w$, respectively. We do not use the event-driven method,[50] often preferred for granular systems at low density, but use instead a time-driven algorithm.[51] The latter is more appropriate for our dense system, where an event-driven approach would require a large number of computations to predict the time of the next particle–particle and particle–wall collision.[46] Since the rod in experiments has a complicated shape (see Fig. 1a), several calculations are required to detect the collisions between the rods. Therefore, in order to simplify the collision rules and speed up the collision detection process, we construct the rod as an array of overlapping spheres (see Fig. 1b).

The ballistic motion of the particles is governed by Newtonian rigid-body dynamics. The Impulse-Based Rigid Body Collision Model[52,53] is implemented to calculate post-collision velocities for all the collisions. We write an MPI-based parallel code to simulate our system: the simulation box is divided into many equal-sized sub-boxes and the dynamics of the particles in different sub-boxes are dealt with by different computer cores. At each step, data for the particles at the boundaries of each sub-box are communicated to the neighbour sub-boxes to execute the collisions between the particles across the sub-boxes. We use VMD software[54] to construct all the simulation movies and snapshots. To achieve the best imitation of the single-particle dynamics of rods and the beads in experiments, we choose the following values of restitution and friction coefficients μ and e (Table 1): we choose the size of the spheres such that the rod in simulations is a close mimic of the original rod in experiments: the tail of the rod is made of seven spheres of 1.1 mm diameter, and the head and the middle parts each consist of three spheres of diameter 0.72 mm and 0.88 mm, respectively (see Fig. 1b). The beads are represented by spheres of diameter 0.8 mm. The mass densities of the rods and beads are 8.7 gm cm^{-3} and 2.7 gm cm^{-3} corresponding to brass and aluminium, respectively. The values of w, f and a_0 are set to 1.2 mm, 200 Hz and 0.04 mm, respectively, as in experiments. In experiments, imperfections in the shape of the rods and the substrate roughness lead to the diffusive nature of the orientation of the rods. Numerical simulations lack such imperfections.

Table 1 Values of restitution and friction coefficients

Collision	μ	e
Particle–particle	0.05	0.3
Rod-base (or lid)	0.03	0.1
Rod-boundary	0.01	0.3
Bead-wall (base, lid or boundary)	0.01	0.3

Therefore, we supply the rods with noisy angular velocity $\omega_z = \varepsilon v_{\text{rel}} \eta$ in the z direction each time they collide with the base or the lid. Here, v_{rel} is the relative velocity at the contact point normal to the contact plane, ε is a control parameter and $\eta = \pm 1$ with equal probability. Fig. 1c shows that the orientation auto-correlation function $C(t)$ of a single rod decays exponentially with time t, and the relaxation time τ decreases with ε, as $\sim \varepsilon^{-2}$ (see Fig. 1d). The value of ε is set to 0.015, as in ref. 35.

3 Results

We first present our findings based on the numerical simulations and then discuss the bands seen in our experiments. In the rest of the paper, all lengths are scaled by the rod length ℓ.

3.1 Simulations

The simulations are performed with the periodic box of dimension $L = 56\ell$ unless otherwise mentioned. The largest systems we studied had $L = 112\ell$, with 7200 rods and 300 000 beads. We here discuss the observed phase diagram (see Section 3.1.1), examine the ordering transition at small Φ_b (see Section 3.1.2), study the properties of bands (see Section 3.1.3), and then present the sound wave spectrum (see Section 3.1.4) and large density fluctuations (see Section 3.1.5) in the highly ordered phase.

3.1.1 Phase diagram. Fig. 2a, a phase diagram in the plane of Φ_r and Φ_b, gives an overview of the behaviour of the system in various regimes. We mainly observe four phases in our system: disordered, homogeneous ordered, banded, and phase-separated (see Fig. 2b–e). The disordered phase, which is found at small values of Φ_r and Φ_b, is structureless at very low rod densities (see Fig. 2b) but displays a few randomly moving highly dense and locally ordered swarms at higher values of Φ_r (see Fig. 11 of the Appendix), presumably incomplete MIPS.[55,56] For $\Phi_r > \Phi_r^c \simeq 0.13$, the band phase is present between the ordered and disordered state (see Fig. 2c). In Section 3.1.3, we present detailed observations on this phase. Ordered states are observed at higher values of Φ_b (see Fig. 2d). The velocity field of the bead medium plays an important role in achieving the ordered state,[35] as can be seen strikingly through a careful choice of initial conditions. When we perform the simulation of a system that is initially at rest, with the rods in an aligned state, the rods immediately start moving with a constant speed but the beads take some time to pick up their steady state in-plane velocity. Therefore, initially, the bead flow is not enough to keep the rods ordered, and the polar order parameter decreases because the rods start disordering. Since they are dragged and pushed by the rods, the beads acquire some speed after some time, and the polar order parameter again increases due to the ordering enhanced by the bead flow (see Fig. 12 of the Appendix). More interestingly, the rods can flock at ultra-low Φ_r (as low as ≈ 0.03) if Φ_b is high enough (see Fig. 13 of the Appendix). At very high densities, phase segregation into bead-rich and (ordered) rod-rich regions is observed (see Fig. 2e and Movie S1, ESI†). This regime occurred in our earlier experiments,[35] where it was characterised as jamming
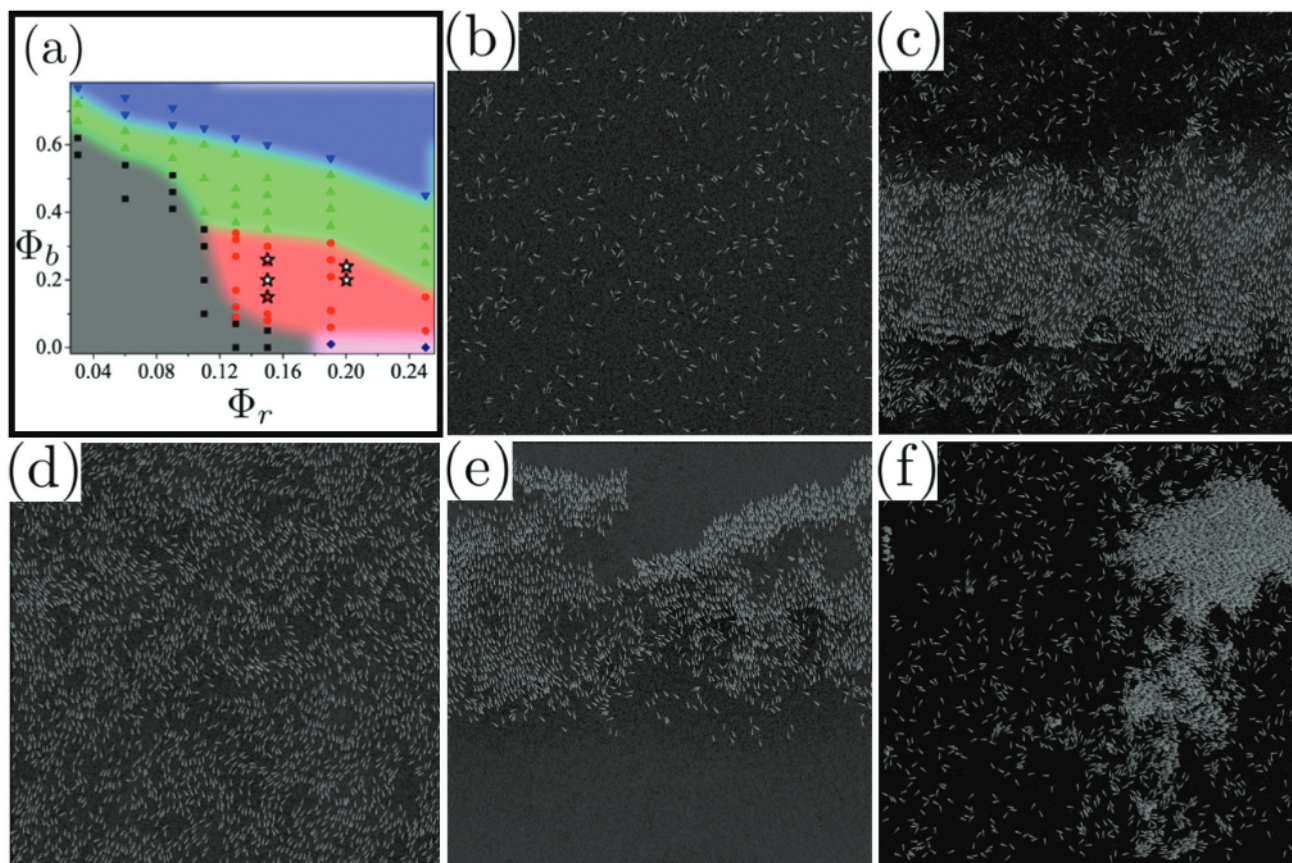
Fig. 2 (a) A phase diagram in the $\Phi_r - \Phi_b$ plane for the system size $L = 56\ell$ (around 228 in diameters of the rod). Here, we find bead–rod phase separation (▼), ordered flock (▲), disordered phase (■), bands (●) and swarms (◆). The stars (☆) depict the location of the band phase in experiments with annular geometry (see Fig. 10). (b) Isotropic state at $\Phi_r = 0.03$ and $\Phi_b = 0.57$. (c) A band, dense in rods and beads, surrounded by the isotropic state at $\Phi_r = 0.19$ and $\Phi_b = 0.21$. (d) A homogeneous ordered state at $\Phi_r = 0.19$ and $\Phi_b = 0.51$. (e) Bead–rod phase separation at very high density ($\Phi_r = 0.15$ and $\Phi_b = 0.60$). Dark background is dense with beads. (f) Possible interplay of alignment and motility-induced phase separation at $\Phi_r = 0.19$ and a very low $\Phi_b = 0.01$.

because the motile rods were immobilised as they pushed up against the sample boundary. A detailed study of the system in this regime will be presented in a separate paper. At higher values of Φ_r ($\gtrsim 0.19$), the rods are condensed into large dense ordered swarms for $\Phi_b \ll 1$, through a MIPS-like mechanism (see Fig. 2f).

Finite-size effects are significant in our study. The observed value of Φ_r^c and the boundaries of the phases are influenced by system size L. We find that Φ_r^c decreases as L is increased but we find no banded state at $\Phi_r = 0.06$ even for system size as big as $L = 112\ell$ (or around 457 rod diameters). We do not pursue the question of whether Φ_r^c can reach zero for very large systems, as seen in agent based numerical simulations.[14]

3.1.2 Phase transition at low Φ_r. In order to measure the ordering of the rods, we first define the order parameter of the rods as $P \equiv |\langle \mathbf{n}_i(t) \rangle|$, where $\mathbf{n}_i(t)$ is the orientation unit vector of the ith rod and $\langle \rangle$ denotes the average over all rods and many configurations in the steady state. Our simulations suggest a direct disorder-to-order phase transition without bands at low $\Phi_r(< \Phi_r^c)$, although we cannot strictly rule out bands on a much larger length scale. In Fig. 3a, we plot the order parameter P as a function of Φ_b for $\Phi_r = 0.03, 0.06, 0.09$ and 0.11. P visibly

increases with Φ_b. In Fig. 3b, P is plotted as a function of Φ_b for $L = 28, 42, 84$ and 112, at $\Phi_r = 0.06$. The profile becomes sharper with increasing L and the graphs for different L don't intersect with each other; this is consistent with a continuous phase transition, but our size range is too limited to conclude further. We now calculate the polar order parameter correlation function defined as $G(r) \equiv \langle \mathbf{n}_i(t) \cdot \mathbf{n}_j(t) \rangle_r$. Here, the averaging is performed over all the pairs of the rods separated by distance r. Fig. 3c, which shows $G(r)$ vs. r for different values of Φ_b at $\Phi_r = 0.06$ and $L = 112$, illustrates that $G(r)$ decays to a nonzero constant at high Φ_b corresponding to long range order, and vanishes for large r at low Φ_b in disordered states.[35] Thus, our numerical experiments are consistent with long-range order in two dimensions, as argued by Toner et al.[40,41]

3.1.3 Properties of bands. At high rod densities ($\Phi_r \geq \Phi_r^c$), a phase is seen between the order and the disordered states in which a single highly ordered and highly dense stripe of the rods and the beads extended over the length of the simulation box – a band – is observed to be moving perpendicular to its own long axis, amidst a disordered background also consisting of a bead–rod mixture (see Fig. 2e, and Movie S2, ESI†). In this system, up to $L = 112$, the segregation results in a single band
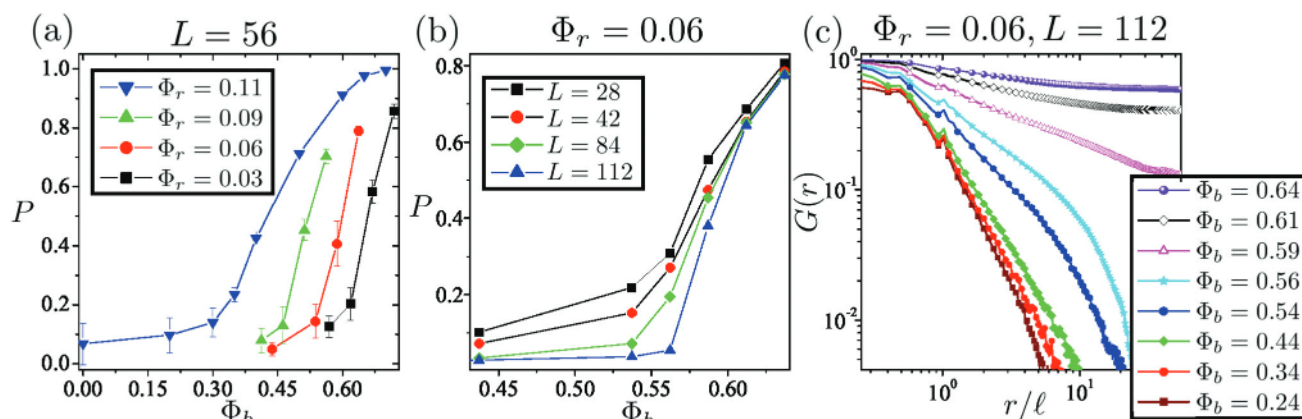
Fig. 3 (a) Order parameter P as a function of rod area fraction Φ_b for Φ_r = 0.03, 0.06, 0.09 and 0.11. (b) P vs. Φ_b for different system sizes at Φ_r = 0.06. (c) Behaviour of $G(r)$ as a function of r for the largest system size ($L = 112\ell$ or 457 rod diameters).

unlike the periodically arranged many bands demonstrated by Vicsek particles.[12,14,57] The bands are generally aligned along the sides of the simulation box but also could be in an arbitrary direction at large values of Φ_r (see Fig. 14 of the Appendix). For convenience of analysis, we study the regime in which the bands are parallel to the length of the simulation box. Let $\mathbf{R}_i^r$ (t) and $\mathbf{R}_i^b(t)$ be the positions of the ith rod and the ith bead, respectively, and $\mathbf{V}_i(t)$ be the velocity of the ith bead, at time t. Respectively, the coarse grained number densities for the rods and beads are defined as

$$\sigma(\mathbf{r}, t) = \frac{1}{l^2}\int_{\text{cell}} \text{d}^2r \sum_i \delta(\mathbf{r} - \mathbf{R}_i^r(t)), \qquad (1)$$

$$\rho(\mathbf{r}, t) = \frac{1}{l^2}\int_{\text{cell}} \text{d}^2r \sum_i \delta(\mathbf{r} - \mathbf{R}_i^b(t)), \qquad (2)$$

where $\sum$ stands for a sum over all the particles and the integration is taken over a square cell of length l centred at position $\mathbf{r}$. Similarly, the polar order parameter field for the rods and the velocity field for the beads are given by

$$\mathbf{p}(\mathbf{r}, t) = \frac{1}{l^2\sigma(\mathbf{r}, t)}\int_{\text{cell}} \text{d}^2r \sum_i \delta(\mathbf{r} - \mathbf{R}_i^r(t))\mathbf{n}_i(t), \qquad (3)$$

$$\mathbf{v}(\mathbf{r}, t) = \frac{1}{l^2\rho(\mathbf{r}, t)}\int_{\text{cell}} \text{d}^2r \sum_i \delta(\mathbf{r} - \mathbf{R}_i^b(t))\mathbf{V}_i(t). \qquad (4)$$

In order to quantify the density and ordering profile of the rods, we define $\phi_r(x) = \langle\sigma(\mathbf{r},t)\rangle$ and $\mathcal{P}(x) \equiv (\mathcal{P}_x(x), \mathcal{P}_y(x)) = \langle\mathbf{p}(\mathbf{r}, t)\rangle$, where we assume that the band is moving along the X axis and the angle bracket represents the average over the Y direction and time in a frame moving with the band. Similarly, the density profile and the velocity profile of the beads are measured by $\phi_b(x) = \langle\rho(\mathbf{r},t)\rangle$ and $\mathcal{V}(x) \equiv (\mathcal{V}_x(x), \mathcal{V}_y(x)) = \langle\mathbf{v}(\mathbf{r}, t)\rangle/\max[|\langle\mathbf{v}(\mathbf{r}, t)\rangle|]$. We divide the simulation box into cells of length one to calculate the value of these functions. A graphical representation of the bands can be found in Fig. 4a showing the typical density profile of the rods in a band moving in the X direction: the scaled density profile of the rods $\phi_r'(x) \equiv \phi_r(x)/\max[\phi_r(x)]$ decays faster at the front than at the back, i.e., the band is asymmetric with the

front sharper than the back. The value of $\mathcal{P}_x(x)$ is close to 1 in the band region and fluctuates around 0 elsewhere, and $\mathcal{P}_y(x)$ remains close to zero everywhere in the simulation box, indicating that the rods in the band region are aligned along the direction of the motion of the band and randomly oriented elsewhere. An interesting feature of these bands is that even the medium particles, the beads, form bands co-centred with the band of the rods (see Fig. 4b), which is an aspect that cannot arise in the related colloidal rollers.[33] In Fig. 4c, we plot $(\mathcal{V}_x(x), \mathcal{V}_y(x))$ and $(\mathcal{P}_x(x), \mathcal{P}_y(x))$ as a function of x, for Φ_r = 0.15 and Φ_b = 0.10. Again, in the band region, the average velocity of beads is high along the direction of the band and vanishingly small elsewhere. Also, the profile of $\mathcal{V}(x)$ is quite similar to that of $\mathcal{P}(x)$. We further explore the effect of Φ_r and the total area fraction $\Phi_t = \Phi_r + \Phi_b$ on the bands. The band becomes wider and denser with increasing Φ_r at fixed Φ_t (see Fig. 4d). The condensation of the particles in a single band has also been observed in the active Ising systems,[14,43] but, in contrast, more than one band was observed in Vicsek systems[14] with the number of bands increasing with system size and particle density. The velocity of the bands v_{band} does not change significantly with Φ_r but the average velocity of the rods lying in the band region v_r increases, probably because of the suppression of the transverse fluctuations of the orientation of the rods due to the increasing density in the band region (see Fig. 4e). The band moves faster than the rods occupying the band because of the significant velocity gradient at its boundaries. For a given value of Φ_r, the band widens with increasing Φ_b, suggesting a tendency to dissolve the band into a homogeneous ordered state at high enough Φ_b (see Fig. 4f). Correspondingly, v_r decreases with Φ_b due to an enhancement in the transverse fluctuations and v_{band} rises due to a decrease in the density gradient across the band boundaries (see Fig. 4g). A shoulder-like trend is found in $G(r)$ vs. r as a result of the rectangular shape of the bands, indicating the typical width of the band (see Fig. 15 of the Appendix). The nature of the phase transition at the boundaries of the segregated regime remains unclear.

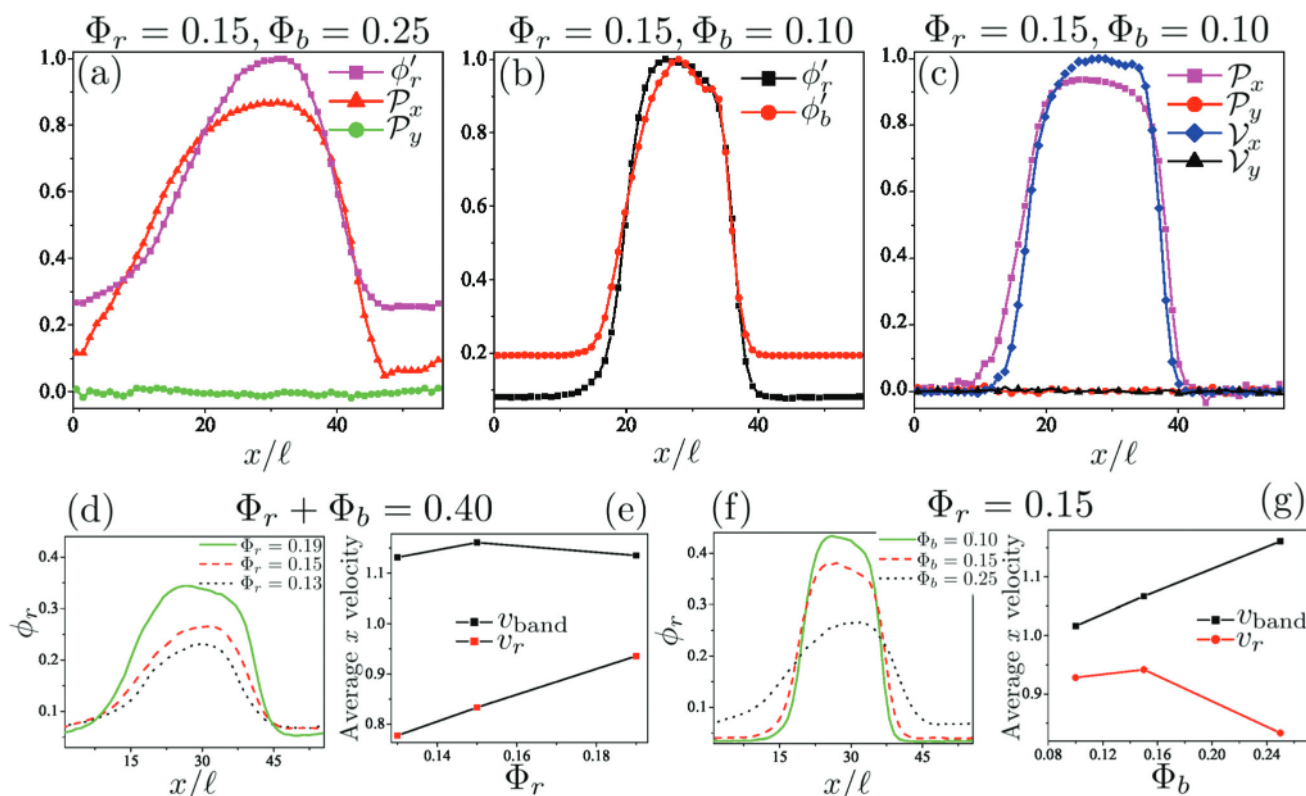Bands in our system do not appear to arise through the instability proposed in ref. 42. Movie S2 (ESI†) suggests a

Fig. 4 Characteristics of the bands moving in the x direction. (a) Scaled density profile $\phi_r'(x) \equiv \phi_r(x)/\max[\phi_r(x)]$ and ordering profile $\mathcal{P}(x)$ of the rods for the band at $\Phi_r = 0.15$ and $\Phi_b = 0.25$. (b) Scaled density profile for the rods and the beads $\phi_r'(x)$ and $\phi_b'(x) \equiv \phi_b(x)/\max[\phi_b(x)]$ at $\Phi_r = 0.15$ and $\Phi_b = 0.10$. (c) Ordering profile of the rods $\mathcal{P}(x)$ and the velocity profile of the beads $\mathcal{V}(x)$ at the parameter values as in (b). At $\Phi_r + \Phi_b = 0.40$, for different values of Φ_r: (d) the rod density profile $\phi_r(x)$ for different values of Φ_r, and (e) the average velocity of the bands v_{band} and the average velocity of their constituent rods v_r as a function of Φ_r. At $\Phi_r = 0.15$, for different values of Φ_b: (f) the rod density profile $\phi_r(x)$ for different values of Φ_b. (g) v_{band} and v_r as a function of Φ_b. Here, $L = 56$.

different mechanism. Initially, small swarms with internal alignment are observed, moving randomly in the isotropic

Fig. 5 Banded structure seen in the simulations with the annular geometry having the same outer boundary as that in our experiments. Here, $\Phi_r = \Phi_b = 0.20$.

background, with both rods and beads joining and leaving them at their boundary. When the swarms come alongside one another, they unite through lateral exchange of particles to form a band.

Our simulations with a long periodic channel of size $14\ell \times 224\ell$ find a single band at $\Phi_b = \Phi_r = 0.20$, which sometimes "calves" a second band that then dissolves (see Movie S3, ESI†). We cannot however rule out multiple bands on an even longer length scale.[14]

In order to explore the possibility of the bands in experiments, we execute simulations with the annular geometry and the outer boundary the same as in our experiments.[35] Fig. 5 and Movie S4 (ESI†) show that the bands should be seen in experiments as well. We will present our experimental result on the bands in subsection 16.

3.1.4 Wavelike excitations. For a statistical characterisation of excitations in the ordered phase, we calculate the dynamic and static orientation structure factors. Let $\mathbf{n}_i^\perp(t)$ be the component of the orientation of the ith rod normal to the direction of the flock. The field for the normal orientation fluctuations is then given by

$$\delta\mathbf{p}_\perp(\mathbf{r}, t) = \frac{\sum_i \mathbf{n}_i^\perp(t)\delta(\mathbf{R}_i^r(t) - \mathbf{r})}{\sum_i \delta(\mathbf{R}_i^r(t) - \mathbf{r})}, \tag{5}$$

where the sum is taken over all the rods. The static orientation structure factor $S_0(\mathbf{q})$ is defined as

$$S_0(\mathbf{q}) = \frac{1}{N}\langle \delta\mathbf{p}_\perp(\mathbf{q}, t) \cdot \delta\mathbf{p}_\perp(-\mathbf{q}, t)\rangle_t, \qquad (6)$$

where $\langle\,\rangle_t$ stands for average over time t and

$$\delta\mathbf{p}_\perp(\mathbf{q}, t) = \sum_i \mathbf{n}_i^\perp(t)\exp(-i\mathbf{q}\cdot\mathbf{R}_i^{\mathrm{r}}(t)) \qquad (7)$$

is the Fourier transform of $\delta\mathbf{p}_\perp(\mathbf{r},t)$ in space. The expression for the dynamic orientation structure factor $S(\mathbf{q},\omega)$ reads

$$S(\mathbf{q}, \omega) = \frac{1}{N}\langle \delta\mathbf{p}_\perp(\mathbf{q}, \omega) \cdot \delta\mathbf{p}_\perp(-\mathbf{q}, -\omega)\rangle, \qquad (8)$$

where the angle bracket stands for an average over time or configuration and $\delta\mathbf{p}_\perp(\mathbf{q},\omega)$ is the Fourier transform of $\delta\mathbf{p}_\perp(\mathbf{q},t)$ in time:

$$\delta\mathbf{p}_\perp(\mathbf{q}, \omega) = \int_t dt \exp(i\omega t)\sum_i \mathbf{n}_i^\perp(t)\exp(-i\mathbf{q}\cdot\mathbf{R}_i^{\mathrm{r}}(t)). \qquad (9)$$

In Fig. 6a, $S(\mathbf{q},\omega)$ vs. ω is reported for modes with wavevectors $\mathbf{q}$ parallel and antiparallel to the directions $\theta = 0$, $\pi/3$ and $\pi/2$ with respect to the flocking direction, for $\Phi_\mathrm{r} = 0.11$, $\Phi_\mathrm{b} = 0.60$ and $L = 112$. We also construct the heat maps for $S(\mathbf{q},\omega)$ as functions of q and ω along these three directions (see Fig. 6b): the single mode for $\theta = 0$ and two modes for the other cases are clearly visible. Correspondingly, $S(\mathbf{q},\omega)$ as a function of ω shows two peaks in all the directions, which merge into one along the direction of the flock. The heat map for the static structure factor for orientation $S_0(\mathbf{q})$ is presented in the bottom-right panel of Fig. 6b, which reveals that the waves are highly anisotropic. Fig. 6c shows that $S_0(\mathbf{q})$ scales as $q^{-\alpha}$ with $\alpha = \alpha_\parallel = 2$ and $\alpha = \alpha_\perp = 1.25$ along and normal to the flock, respectively. These exponent values are consistent with Toner–Tu theory,[8] which predicts $\alpha_\parallel = 2$ and $\alpha_\perp = 1.2$ but differ from the values $\alpha_\parallel = 1.4$ and $\alpha_\perp = 1.33$ calculated from the large-scale simulations of the Vicsek model.[58] The speed of the propagating mode of wave vector $\mathbf{q}$ is defined as

$$v_\mathrm{s}(\mathbf{q}) = \omega_\mathrm{p}(\mathbf{q})/q, \qquad (10)$$

where $\omega_\mathrm{p}(\mathbf{q})$ is the position of the peak corresponding to the mode in the $S(\mathbf{q},\omega)$ vs. ω plot. We find that ω_p is proportional to q for small q (see Fig. 7a, b and c for $\theta = 0$, $\pi/3$ and $\pi/2$, respectively), except where $v_\mathrm{s}(q = 0)$ is very small, e.g., wavevectors at $4\pi/3$ to the flocking direction. The width of the peak $\Delta\omega(\mathbf{q})$ displays a dependence consistent with a power law q^β. The value of β is $\beta_\parallel = 1.6$ for $\theta = 0$, 0.6 and 0.9 for the two peaks at $\theta = \pi/3$ and $\beta_\perp = 0.6$ for both the peaks at $\theta = \pi/2$ (insets of Fig. 7a–c). This is in contrast to the Toner–Tu[8] prediction $\beta_\parallel = 2$ and $\beta_\perp = 1.2$ as well as $\beta_\parallel = 1.4$ and $\beta_\perp = 1.33$ found in the large-scale simulation studies of the Vicsek model.[58] Fig. 7d shows the angular dependence of $v_\mathrm{s}(\theta)$ at $q = 45(2\pi/L)$. Two loops intersecting at $\theta = 0$ correspond to two wave modes. All these observations agree reasonably with the theoretical predictions[8] except the wavenumber dependence of the sound peak widths. The broken-symmetry "sound" waves have already been detected in the numerical simulations of Vicsek-style models[9]
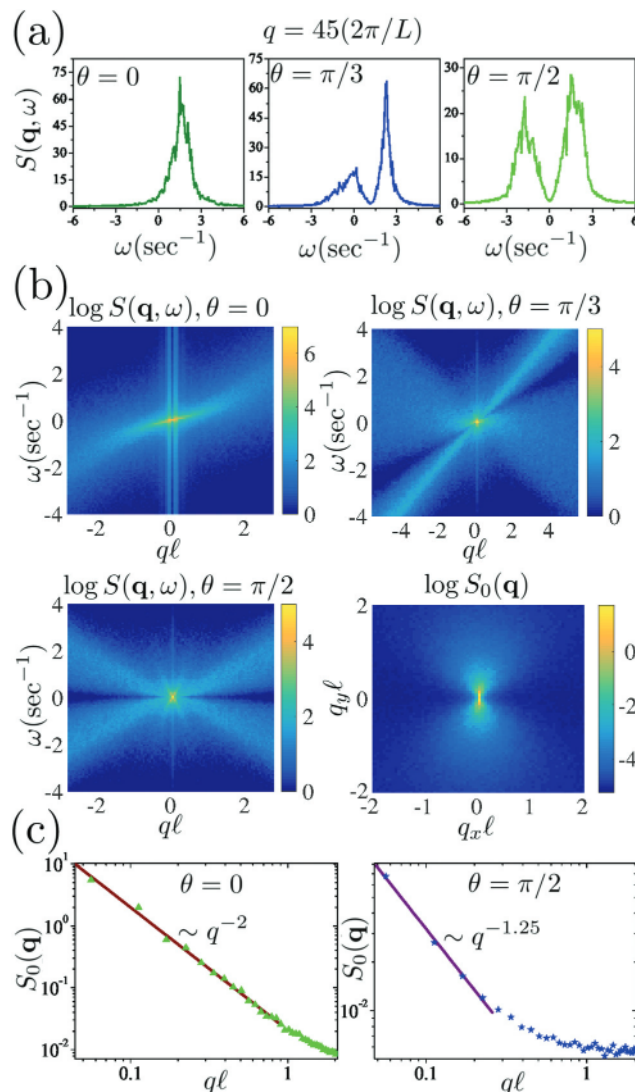

Fig. 6 (a) $S(\mathbf{q},\omega)$ vs. ω for $q = 45(2\pi/L)$ at angles $\theta = 0$, $\theta = \pi/3$ and $\theta = \pi/2$ along the direction of the flock. (b) Heat map of $\log S(\mathbf{q},\omega)$ as a function of q and ω at the three different angles the same as in (a), and the heat map of the static structure factor $\log S_0(\mathbf{q})$ as the function of q_x and q_y. (c) $S_0(\mathbf{q})$ vs. q for $\theta = 0$ and $\theta = \pi/2$: $S_0(\mathbf{q})$ scales as $q^{-\alpha}$ with $\alpha = 2$ and $\alpha = 1.25$ for $\theta = 0$ and $\theta = \pi/2$, respectively. Here, the flock is moving along the x direction. Parameter values: $\Phi_\mathrm{r} = 0.11$, $\Phi_\mathrm{b} = 0.60$ and $L = 112$.

but observing them in our numerical model, which is mechanically realistic rather than agent-based, suggests that these modes should play a significant role in real granular-matter experiments. Given both the limited dynamic range of wavenumbers in our study and the observed disagreement between Toner–Tu theory and the presumably definitive numerical measurements[58] on the Vicsek model, we will not dwell further on the issue of the scaling of sound-peak widths here.

A different wavelike aspect is seen in Movie S5 (ESI†), for $\Phi_\mathrm{r} = 0.19$ and $\Phi_\mathrm{b} = 0.51$, in the form of undulating structures,[59] with considerable lateral wandering, on a uniform ordered background. These do not appear to be phase-coherent, and the measurements of $S(\mathbf{q},\omega)$ do not show peaks corresponding to oscillations at an intrinsic, system-size-independent frequency.
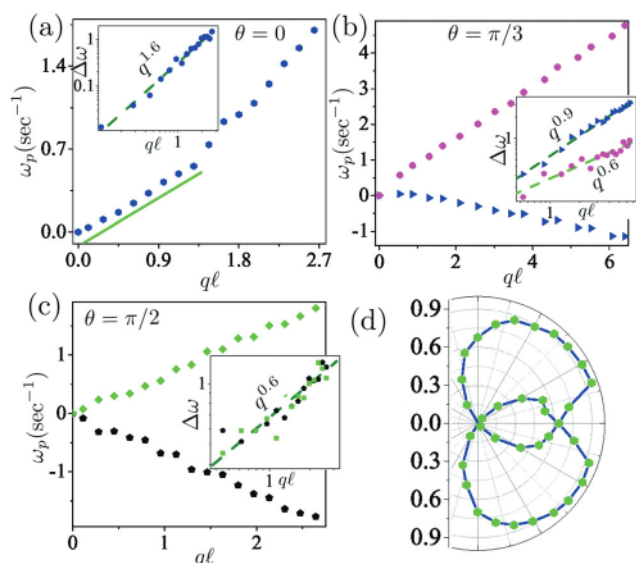
Fig. 7 (a)–(c) show $\omega_p(\mathbf{q})$ vs. q for the wavevector $\mathbf{q}$ parallel and anti-parallel to the directions $\theta = 0$, $\pi/3$ and $\pi/2$ with respect to the flocking direction. The insets show peak width $\Delta\omega(\mathbf{q}) \propto q^{\beta}$, with $\beta = 1.6$ for $\theta = 0$, $\beta = 0.6$ and 0.9 for $\pi/3$, and $\beta = 0.6$ for $\pi/2$. (d) A polar plot presenting the measured speed of the sound modes as a function of angle θ of the propagation vector along the direction of the flock, calculated at $q = 45(2\pi/L)$. Considerable dispersion is seen for $\mathbf{q}$ antiparallel to $\pi/3$ as the speed at $q = 0$ is small. Here, $\Phi_r = 0.11$, $\Phi_b = 0.60$ and $L = 112$.

However, their presence suggests an incipient excitability of the uniform flock towards oscillations, which we propose to explore further through our numerical studies and by examining the Toner–Tu equations in the regime of bending instabilities.[60]

3.1.5 Large density fluctuations. In the thermal equilibrium systems away from critical points, in the thermodynamic limit, the particle number fluctuations in the grand canonical ensemble grow as the square root of the average number of the particle $\langle N \rangle$ as the system size is increased, i.e. root-mean-square deviation

$$\Delta N = \sqrt{\langle N^2 \rangle - \langle N \rangle^2} \propto \langle N \rangle^{1/2}, \qquad (11)$$

where N is the instantaneous number of the particles and $\langle \rangle$ represents the ensemble average for a given system size. In contrast, active systems show anomalous number fluctuation properties: hydrodynamical theories[5,8,15] suggest that ΔN for active polar and apolar systems is proportional to $\langle N \rangle^{1/2}$ in isotropic states but the broken-symmetry states demonstrate large number fluctuations growing as[5,8,15]

$$\Delta N \propto \langle N \rangle^{\eta + \frac{1}{2}}, \qquad (12)$$

where $\eta = 1/d$ in mean field theory and has smaller values in renormalization-group treatments of active polar[8] and nematic[61] phases. We construct a series varying the number of particles inside subsystems of different sizes co-centred with the original system, from many statistically independent realizations. We then calculate $\langle N \rangle$ and ΔN for each subsystem. At low Φ_r, in the disordered isotropic state, ΔN is proportional to $\langle N \rangle^{1/2}$
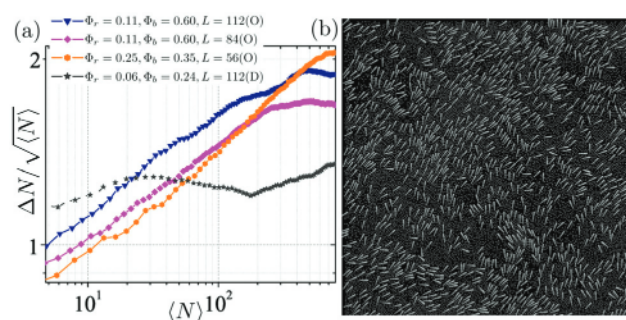

Fig. 8 (a) Variance in the number of rods scaled by $\sqrt{\langle N \rangle}$ vs. the average number of rods $\langle N \rangle$ for three ordered states (labelled O) and one disordered state (labelled D). (b) Snapshot of the ordered state at $\Phi_r = 0.25$ and $\Phi_b = 0.35$ at $L = 56$.

(see Fig. 8a for $\Phi_r = 0.06$ and $\Phi_b = 0.24$). Fig. 8a presents $\Delta N/\sqrt{\langle N \rangle}$ vs. $\langle N \rangle$ for three different ordered states: the number fluctuations are larger than the thermal systems with $a \sim 0.6$ but weaker than the ones predicted by Toner–Tu theory. More detailed studies with finite-size scaling are required for a definitive exponent estimate. Here, we should make it clear that the large number fluctuations in order states are not due to a segregation as seen in Fig. 2e and h: a typical ordered state has homogenous rod density (see Fig. 8b).

In order to quantify the lifetime of the number fluctuations, we also calculate the density autocorrelation function defined as

$$C_\sigma(t) = \langle (\sigma(\mathbf{r},t) - \sigma_0(\mathbf{r}))(\sigma(\mathbf{r},0) - \sigma_0(\mathbf{r})) \rangle, \qquad (13)$$

where $\sigma_0(\mathbf{r})$ is the average density at position $\mathbf{r}$ and $\langle \rangle$ represents the average over space. The coarse-grained number density for the rods $\sigma(\mathbf{r},t)$ has been defined in Section 3.1.3. Fig. 9 suggests that $C_\sigma(t)$ shows two exponential decays. We do not understand this observation. A linearized treatment by Narayan et al.[6] would give a logarithmic decay, while Toner–Tu theory[8] would give a slower $t^{-2/3}$ in two dimensions. Neither of these forms gives a reasonable fit to our data. The finite size effects could be the reason we do not see agreement with the existing theories.

3.2 Experiments

As we showed in earlier work,[35] a flocking transition can be triggered at very low area fraction of motile polar rods by increasing the concentration of non-motile beads (see Fig. 16 of the Appendix). Here, motivated by our simulations, we perform experiments in annular geometry at varying Φ_b and Φ_r and find that for parameter values shortly after the onset of flocking, a band does emerge, with appearance typically as in Fig. 10b–f and Movie S6 (ESI†). The band is identified as the area of high density of rods and beads with a high degree of orientational order that is moving in the direction of its order, with a background of an isotropic mixture with a low concentration of both rods and beads. Fig. 10 indicates that, at fixed Φ_r, the band becomes wider as Φ_b increased, which is consistent with our simulation results. The location of the bands in the $\Phi_r - \Phi_b$ plane is depicted in the phase diagram in Fig. 2a. Although the observation of band formation in our experiments
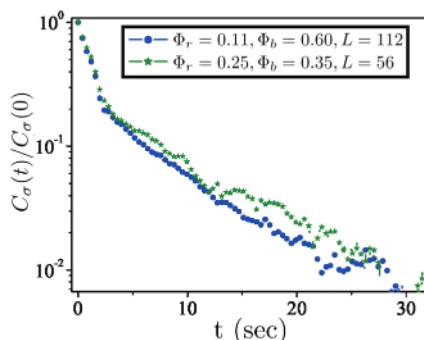
Fig. 9 Density autocorrelation function $C_\sigma(t)$ scaled by its value at $t = 0$ as a function of t. Here, $\Phi_r = 0.11$, $\Phi_b = 0.60$ and $L = 112$ and the size of the cell used for coarse-graining is 2ℓ.

is robust, limitations on system size make a more systematic study impractical.

4 Future directions and summary

The research presented in this article was motivated by multiple aims. One was to study collective motion with both self-propulsion and alignment arising for purely mechanical rather than behavioural reasons. The second was to carry out such a study in a system in which – unlike in the Quinke rollers[33] – the strength of interactions could be tuned simply, in this case by changing the bead concentration. Third was to see if the band formation just after the ordering onset could be modulated or suppressed. Despite the limitations on system size, we believe we have succeeded in achieving the above aims. Two regimes remain to be explored in more detail. One is the limit of no beads, not discussed here, where a patchy MIPS precursor possibly leads to a dilute flock at low noise (see Fig. 17 of the Appendix and Movie S7, ESI†). The other is the bead–rod phase separation that occurs at a high area fraction of both species.

We close with a summary. In our detailed numerical simulations, we observed four distinct phases of our system: disordered, banded and ordered, homogeneous and ordered, and bead–rod phase separated. The existence of the broken symmetry state at very low rod concentration is a key result. The banded state is similar to the one seen in a system of polar disks[13] or in rolling colloids:[33] only single bands are observed, which are generally aligned with the boundary of the periodic box but also could be in an arbitrary direction at high rod concentration. Moreover, in these systems, the band absorbs the bead medium as well, for which there is no equivalent in the other systems like polar disks and colloidal rollers.[33] The width of the bands increases with the rod concentration. We also find the first experimental realisation of bands in a dry granular flocking system. We also explore the anisotropic propagating waves and large number fluctuations in the highly
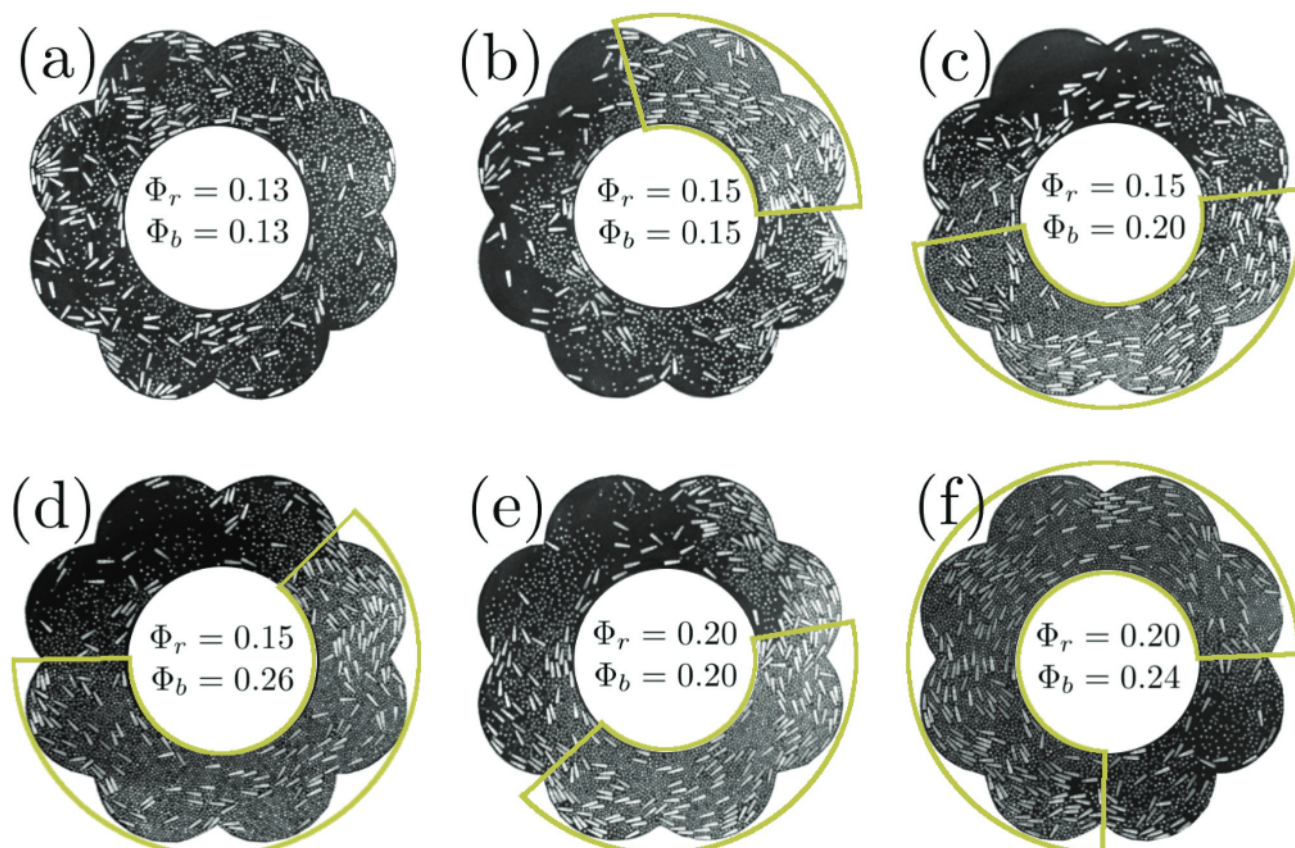

Fig. 10 Images from the experiments performed with rods and beads in annular geometry: (a) an isotropic phase and (b–d) bands at different Φ_r and Φ_b. It can be seen from (b–d) for $\Phi_r = 0.15$, and (e and f) for $\Phi_r = 0.20$, that the size of the band increases with Φ_b, as observed in our simulations.

ordered state. Some interesting departures are observed with respect to Toner–Tu theory,[8] especially as regards the scaling of damping rate with wavenumber.
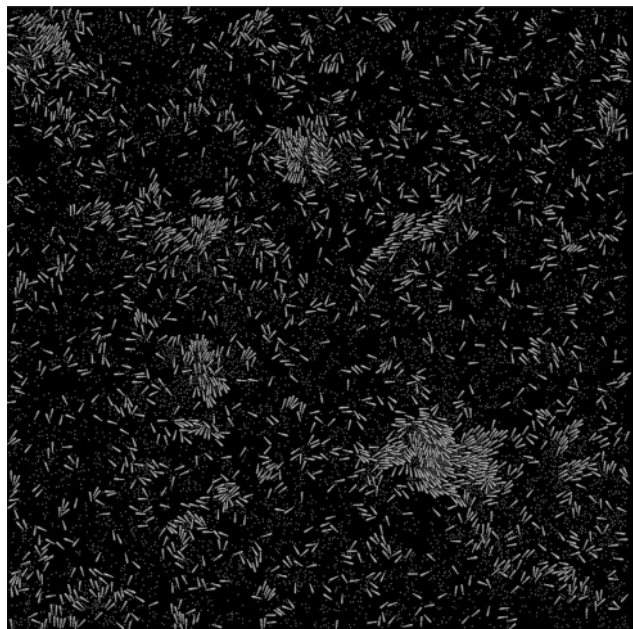
Appendix

Fig. 11 A disordered phase at low Φ_b and high Φ_r having locally ordered swarms. Here, $\Phi_r = 0.13$ and $\Phi_b = 0.07$.
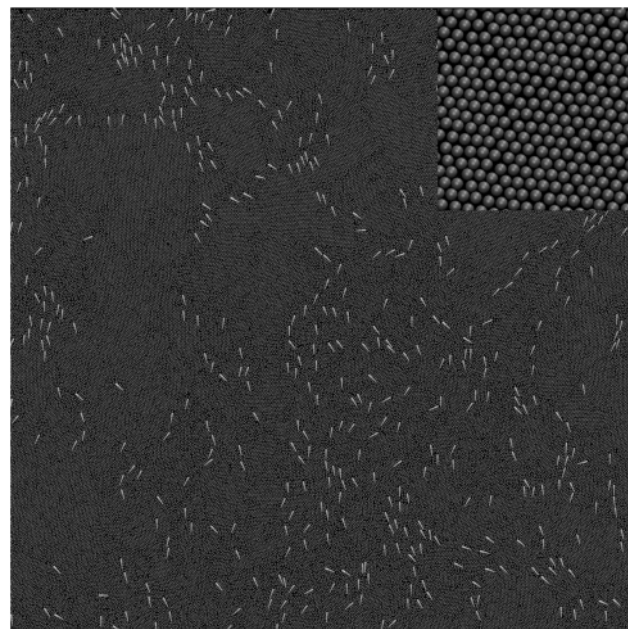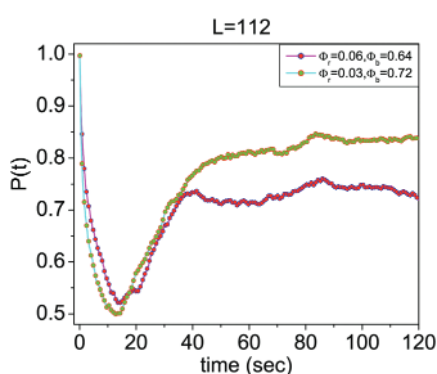

Fig. 12 Time evolution of the polar order parameter $P(t)$ of the system, which is perfectly ordered with zero velocity at $t = 0$. Initially, the ordering of the rods starts lessening due to the absence of the bead flow. In some time, as soon as the beads pick up the velocity as they are pushed and dragged by the rods, the rods begin to realign due to the interaction with the bead flow. Correspondingly, the order parameter $P(t)$ initially decreases and then increases after some time.
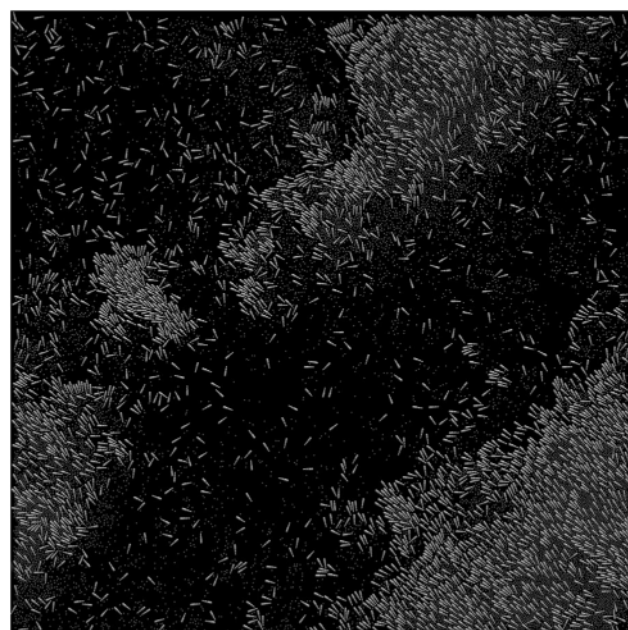
Conflicts of interest

There are no conflicts to declare.

Fig. 13 Ordered state at extremely low rod density $\phi_r = 0.03$ with $\phi_b = 0.72$. The inset shows the crystalline order in the bead medium.

Fig. 14 A band moving in a direction not parallel to the sides of the periodic box at $\phi_r = 0.19$ and $\Phi_b = 0.11$.
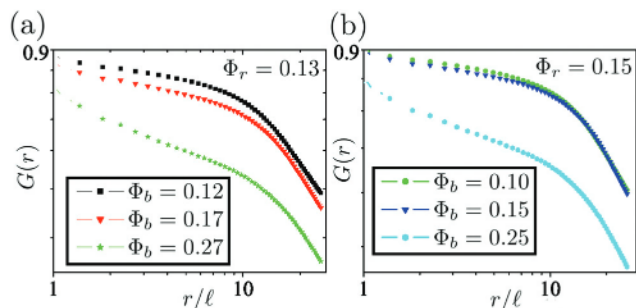
Fig. 15 Order parameter correlation function $G(r)$ vs. r in the band regime of the phase diagram. $\Phi_r = 0.13$ for (a) and $\Phi_r = 0.15$ for (b). System size $L = 56$.
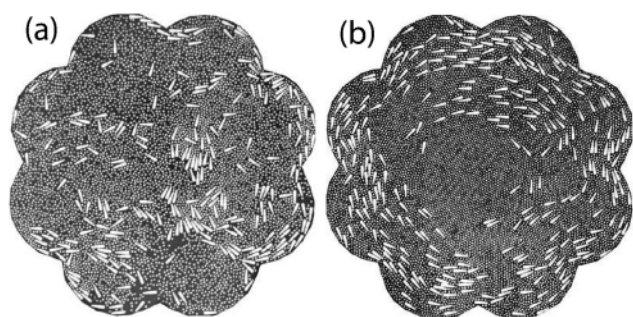

Fig. 16 In experiments, a disordered phase at low Φ_b (left), and an ordered phase at high Φ_b (right) of a system of rods and beads.[35]
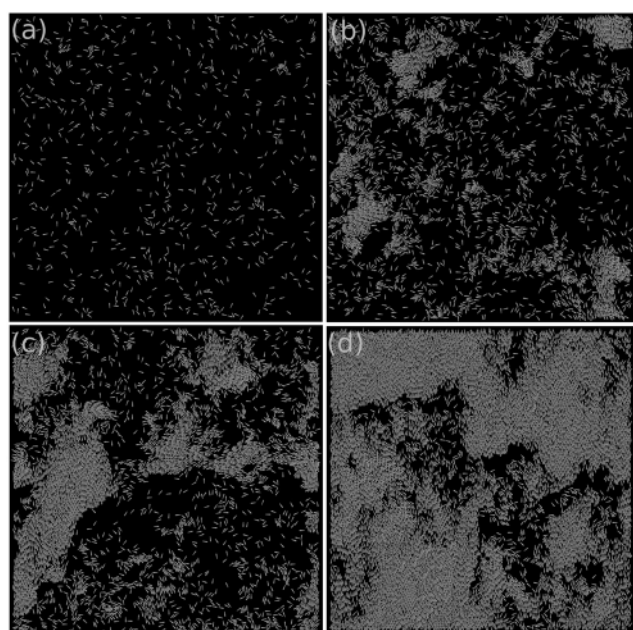

Fig. 17 Behaviour of the system with no beads. (a) Disordered state at $\Phi_r = 0.05$. Patchy swarms at large Φ_r: (b) at $\Phi_r = 0.20$, (c) at $\Phi_r = 0.30$ and (d) at $\Phi_r = 0.60$. Size of the swarms increases with Φ_r.

Notes and references

1 M. C. Marchetti, J. F. Joanny, S. Ramaswamy, T. B. Liverpool, J. Prost, M. Rao and R. A. Simha, *Rev. Mod. Phys.*, 2013, **85**, 1143–1189.
2 S. Ramaswamy, *Annu. Rev. Condens. Matter Phys.*, 2010, **1**, 323–345.
3 J. Toner, Y. Tu and S. Ramaswamy, *Ann. Phys.*, 2005, **318**, 170–244.
4 C. Bechinger, R. Di Leonardo, H. Löwen, C. Reichhardt, G. Volpe and G. Volpe, *Rev. Mod. Phys.*, 2016, **88**, 045006.
5 S. Ramaswamy, R. A. Simha and J. Toner, *EPL*, 2003, **62**, 196.
6 V. Narayan, S. Ramaswamy and N. Menon, *Science*, 2007, **317**, 105–108.
7 V. Narayan, PhD thesis, Indian Institute of Science, 2008.
8 J. Toner and Y. Tu, *Phys. Rev. E: Stat., Nonlinear, Soft Matter Phys.*, 1998, **58**, 4828–4858.
9 Y. Tu, J. Toner and M. Ulm, *Phys. Rev. Lett.*, 1998, **80**, 4819–4822.
10 D. Geyer, A. Morin and D. Bartolo, *Nat. Mater.*, 2018, **17**, 789.
11 J. Toner, 2018, arXiv preprint arXiv:1812.00310.
12 H. Chaté, F. Ginelli, G. Grègoire, F. Peruani and F. Raynaud, *Eur. Phys. J. B*, 2008, **64**, 451–456.
13 C. A. Weber, T. Hanke, J. Deseigne, S. Léonard, O. Dauchot, E. Frey and H. Chaté, *Phys. Rev. Lett.*, 2013, **110**, 208001.
14 A. P. Solon, H. Chaté and J. Tailleur, *Phys. Rev. Lett.*, 2015, **114**, 068101.
15 R. A. Simha and S. Ramaswamy, *Phys. Rev. Lett.*, 2002, **89**, 058101.
16 T. Sanchez, D. T. Chen, S. J. DeCamp, M. Heymann and Z. Dogic, *Nature*, 2012, **491**, 431.
17 L. Giomi, M. J. Bowick, X. Ma and M. C. Marchetti, *Phys. Rev. Lett.*, 2013, **110**, 228101.
18 L. Giomi, M. J. Bowick, P. Mishra, R. Sknepnek and M. Cristina Marchetti, *Philos. Trans. R. Soc., A*, 2014, **372**, 20130365.
19 S. Shankar, S. Ramaswamy, M. C. Marchetti and M. J. Bowick, *Phys. Rev. Lett.*, 2018, **121**, 108002.
20 A. Doostmohammadi, J. Ignés-Mullol, J. M. Yeomans and F. Sagués, *Nat. Commun.*, 2018, **9**, 1–13.
21 N. Kumar, R. Zhang, J. J. de Pablo and M. L. Gardel, *Sci. Adv.*, 2018, **4**, eaat7779.
22 M. E. Cates and J. Tailleur, *Annu. Rev. Condens. Matter Phys.*, 2015, **6**, 219–244.
23 M. Cates, 2019, arXiv preprint arXiv:1904.01330.
24 N. Kumar, R. K. Gupta, H. Soni, S. Ramaswamy and A. Sood, *Phys. Rev. E*, 2019, **99**, 032605.
25 G. S. Redner, M. F. Hagan and A. Baskaran, *Phys. Rev. Lett.*, 2013, **110**, 055701.

26 H. M. López, J. Gachelin, C. Douarche, H. Auradou and E. Clément, *Phys. Rev. Lett.*, 2015, **115**, 028301.

27 A. Sokolov and I. S. Aranson, *Phys. Rev. Lett.*, 2009, **103**, 148101.

28 S. D. Ryan, B. M. Haines, L. Berlyand, F. Ziebert and I. S. Aranson, *Phys. Rev. E: Stat., Nonlinear, Soft Matter Phys.*, 2011, **83**, 050904.

29 D. Bray, *Cell movements: from molecules to motility*, Garland Science, 2000.

30 B. Alberts, D. Bray, J. Lewis, M. Raff, K. Roberts and J. Watson, *Molecular Biology of the Cell*, New York, 3rd edn, 1994, pp. 18–19.

31 F. Jülicher, S. W. Grill and G. Salbreux, *Rep. Prog. Phys.*, 2018, **81**, 076601.

32 S. Saha, R. Golestanian and S. Ramaswamy, *Phys. Rev. E: Stat., Nonlinear, Soft Matter Phys.*, 2014, **89**, 062316.

33 A. Bricard, J.-B. Caussin, N. Desreumaux, O. Dauchot and D. Bartolo, *Nature*, 2013, **503**, 95–98.

34 V. Narayan, N. Menon and S. Ramaswamy, *J. Stat. Mech.: Theory Exp.*, 2006, **2006**, P01005.

35 N. Kumar, H. Soni, S. Ramaswamy and A. Sood, *Nat. Commun.*, 2014, **5**, 4688.

36 A. Cavagna and I. Giardina, *Annu. Rev. Condens. Matter Phys.*, 2014, **5**, 183–207.

37 H. Chaté, *Annu. Rev. Condens. Matter Phys.*, 2020, **11**, 189–212, DOI: 10.1146/annurev-conmatphys-031119-050752.

38 J. Deseigne, S. Leonard, O. Dauchot and H. Chaté, *Soft Matter*, 2012, **8**, 5629–5639.

39 T. Vicsek, A. Czirók, E. Ben-Jacob, I. Cohen and O. Shochet, *Phys. Rev. Lett.*, 1995, **75**, 1226.

40 J. Toner and Y. Tu, *Phys. Rev. Lett.*, 1995, **75**, 4326–4329.

41 J. Toner, *Phys. Rev. Lett.*, 2012, **108**, 088102.

42 E. Bertin, M. Droz and G. Grégoire, *Phys. Rev. E: Stat., Nonlinear, Soft Matter Phys.*, 2006, **74**, 022101.

43 A. P. Solon and J. Tailleur, *Phys. Rev. Lett.*, 2013, **111**, 078101.

44 L. Chen and J. Toner, *Phys. Rev. Lett.*, 2013, **111**, 088701.

45 J.-B. Caussin, A. Solon, A. Peshkov, H. Chaté, T. Dauxois, J. Tailleur, V. Vitelli and D. Bartolo, *Phys. Rev. Lett.*, 2014, **112**, 148102.

46 H. Soni, PhD thesis, Indian Institute of Science, 2015.

47 N. Kumar, PhD thesis, Indian Institute of Science, 2015.

48 A. Maitra, P. Srivastava, M. C. Marchetti, S. Ramaswamy and M. Lenz, *Phys. Rev. Lett.*, 2020, **124**, 028002.

49 J. Deseigne, O. Dauchot and H. Chaté, *Phys. Rev. Lett.*, 2010, **105**, 098001.

50 T. Pöschel and T. Schwager, *Computational granular dynamics: models and algorithms*, Springer Science & Business Media, 2005.

51 *Understanding Molecular Simulation (Second Edition)*, ed. D. Frenkel and B. Smit, Academic Press, San Diego, 2nd edn, 2002, pp. 1–661.

52 W. J. Stronge, *J. Appl. Mech.*, 1994, **61**, 605–611.

53 W. J. Stronge, *Impact Mechanics*, Cambridge University Press, Cambridge, United Kingdom, 2000.

54 W. Humphrey, A. Dalke and K. Schulten, *J. Mol. Graphics*, 1996, **14**, 33–38.

55 M. E. Cates and J. Tailleur, *Annu. Rev. Condens. Matter Phys.*, 2015, **6**, 219–244.

56 In the present context MIPS is simply joint condensation of rods and beads, and should not be confused with the demixing of the two species, which we call segregation, observed at higher area fraction.

57 H. Chaté, F. Ginelli, G. Grégoire and F. Raynaud, *Phys. Rev. E: Stat., Nonlinear, Soft Matter Phys.*, 2008, **77**, 046113.

58 B. Mahault, F. Ginelli and H. Chaté, *Phys. Rev. Lett.*, 2019, **123**, 218001.

59 We thank an anonymous referee for drawing our attention to this feature.

60 L. P. Dadhichi, J. Kethapelli, R. Chajwa, S. Ramaswamy and A. Maitra, *Phys. Rev. E*, 2020, **101**, 052601 (arXiv:1912.06581).

61 S. Shankar, S. Ramaswamy and M. C. Marchetti, *Phys. Rev. E*, 2018, **97**, 012707.